

The star formation main sequence and stellar mass assembly of galaxies in the Illustris simulation

Martin Sparre^{1*}, Christopher C. Hayward^{2,3,†}, Volker Springel^{3,4}, Mark Vogelsberger⁵, Shy Genel⁶, Paul Torrey^{2,5,6}, Dylan Nelson⁶, Debora Sijacki⁷, Lars Hernquist⁶

¹Dark Cosmology Centre, Niels Bohr Institute, University of Copenhagen, Juliane Maries Vej 30, 2100 Copenhagen, Denmark

²TAPIR, Mailcode 350-17, California Institute of Technology, Pasadena, CA 91125, USA

³Heidelberger Institut für Theoretische Studien, Schloss-Wolfsbrunnengasse 35, 69118 Heidelberg, Germany

⁴Zentrum für Astronomie der Universität Heidelberg, Astronomisches Recheninstitut, Mönchhofstrasse 12-14, 69120 Heidelberg, Germany

⁵Department of Physics, Kavli Institute for Astrophysics and Space Research, Massachusetts Institute of Technology, Cambridge, MA 02139, USA

⁶Harvard-Smithsonian Center for Astrophysics, 60 Garden Street, Cambridge, MA 02138, USA

⁷Kavli Institute for Cosmology, Cambridge, and Institute of Astronomy, Madingley Road, Cambridge, CB3 0HA, UK

23 September 2022

ABSTRACT

Understanding the physical processes that drive star formation is a key challenge for galaxy formation models. In this article we study the tight correlation between the star formation rate (SFR) and stellar mass of galaxies at a given redshift, how halo growth influences star formation, and star formation histories of individual galaxies. We study these topics using Illustris, a state-of-the-art cosmological hydrodynamical simulation of galaxy formation. Illustris reproduces the observed relation (the star formation main sequence; SFMS) between SFR and stellar mass at redshifts $z = 0$ and $z = 4$, but at intermediate redshifts of $z \simeq 1 - 2$, the simulated SFMS has a significantly lower normalisation than reported by observations. The scatter in the relation is consistent with the observed scatter. However, the fraction of outliers above the SFR-stellar mass relation in Illustris is less than that observed. Galaxies with halo masses of $\sim 10^{12} M_{\odot}$ dominate the SFR density of the Universe, in agreement with the results of abundance matching. Furthermore, more-massive galaxies tend to form the bulk of their stars at high redshift, which indicates that ‘downsizing’ occurs in Illustris. We also studied the star formation histories of individual galaxies, including the use of a principal component analysis decomposition. We find that for fixed stellar mass, galaxies that form earlier have more-massive black holes at $z = 0$, indicating that star formation and black hole growth are tightly linked processes in Illustris. While many of the properties of normal star-forming galaxies are well-reproduced in the Illustris simulation, forming a realistic population of starbursts will likely require higher resolution and probably a more sophisticated treatment of star formation and feedback from stars and black holes.

Key words: cosmology: theory – methods: numerical – galaxies: evolution – galaxies: formation – galaxies: star formation – galaxies: starburst.

1 INTRODUCTION

In the Λ CDM paradigm, galaxies reside in dark matter halos that are built up hierarchically as gravity amplifies perturbations created in the early Universe (Zel’dovich 1970). The structure and substructure of dark matter halos, and the cosmic web surrounding them, have been intensively studied using numerical simulations (e.g. Springel et al. 2005; Diemand et al. 2008; Klypin et al. 2011), in which the dark matter is modelled as collisionless particles that interact with each other only through gravity. In the last decade,

such simulations have led to a general consensus about the distribution of dark matter on large scales. However, the formation and evolution of the baryons embedded in these halos are far from understood. In the canonical theory of galaxy formation (e.g. Silk 1977; Rees & Ostriker 1977; White & Rees 1978), galaxies form stars when hot gas radiates away energy, cools and loses pressure support. The evolution of such galaxies is further influenced by their merger history, accretion of gas and dark matter, and regulation of star formation by feedback processes related to stellar winds, supernovae and active galactic nuclei. Much of our understanding of galaxies is based on observed relations and physical modelling of galaxy structure. Important observations include the relation between luminosity and velocity widths of galaxies (Faber & Jackson

* E-mail: sparre@dark-cosmology.dk

† Moore Prize Postdoctoral Scholar in Theoretical Astrophysics

1976; Tully & Fisher 1977), the global star formation rate as a function of redshift (Lilly et al. 1996; Madau et al. 1998), relations between mass and metallicity (Tremonti et al. 2004; Mannucci et al. 2010), global star formation laws (Schmidt 1959; Kennicutt 1998), and the morphologies of galaxies (Hubble 1926; Dressler 1980).

A recently established relation is the so-called ‘star formation main sequence’ (SFMS), which is an approximately linear relation between the star formation rate (SFR) and the stellar mass (M_*) of star-forming galaxies. The relation exists at both low ($z < 1$; Brinchmann et al. 2004; Salim et al. 2007) and high ($z \gtrsim 1$; Daddi et al. 2007) redshift and is recovered in optical, infrared (Elbaz et al. 2011) and radio observations (Karim et al. 2011). It is a tight relation in the sense that the scatter around the relation is small (e.g. Speagle et al. 2014 reports a scatter of $\sigma \simeq 0.2$ dex). The normalisation of the SFMS is observed to increase from $z = 0$ to $z = 2$, the redshift at which the global star formation rate density peaks. The tightness of the SFMS and the fact that most star-forming galaxies lie on it imply that the bulk of the star formation in the Universe occurs in a quasi-steady state (Noeske et al. 2007) and that the fraction of a given star-forming galaxy’s lifetime during which it lies significantly above the SFMS because of e.g. merger-induced starbursts is small.¹

In addition to characterising star-forming galaxies, the SFMS also provides a natural way to define starbursts as galaxies with SFRs well above the SFMS value for their stellar mass and redshift (Rodighiero et al. 2011; Sargent et al. 2012; Atek et al. 2014). Despite having large SFRs compared with normal galaxies, starbursts account for only a small fraction ($\sim 5 - 10$ per cent) of the global SFR density (Rodighiero et al. 2011) because they are rare and short-lived (because of their short gas-consumption timescales; Knapen & James 2009; Genzel et al. 2010; Daddi et al. 2010). This minor contribution of starbursts to the total SFR density is consistent with semi-empirical models for infrared galaxy number counts (B  thermin et al. 2012) and luminosity functions (Hopkins et al. 2010). ‘Red and dead’ or quiescent galaxies are galaxies that lie significantly below the SFMS. These galaxies are typically elliptical galaxies (Wuyts et al. 2011) with little gas available for star formation. They are likely the descendants of starbursts after their intense star formation has been quenched by feedback from active galactic nuclei (AGN; e.g. Sanders et al. 1988; Toft et al. 2014; Cemile Marsan et al. 2014) or other processes. Because we are interested in actively star-forming galaxies, we will largely ignore the quiescent galaxy population in this work.

Several attempts have been made to reproduce the SFMS in hydrodynamical simulations of galaxies (e.g. Dav   et al. 2011; Torrey et al. 2014) and (semi-)analytical models (e.g. Dutton et al. 2010; Dav   et al. 2012; Dekel et al. 2013). With both methods, a tight relationship between SFR and stellar mass can be recovered. However, reproducing the evolution of the normalisation is a challenge for theoretical models (e.g. Dav   2008; Damen et al. 2009). The main problem is producing the correct normalisation at both

$z = 0$ and $z = 2$. Potential solutions to this problem have been suggested, including a varying IMF (Dav   2008) and modification of the timescale for reincorporation of gas ejected by feedback processes (Mitchell et al. 2014).

A different important characteristic of a population of galaxies is the connection between the growth of halos and the formation of stars inside them. Dark matter halos build up hierarchically through accretion and mergers. The formation of stars is a more complex phenomenon that is heavily influenced by feedback processes and gas cooling. By matching the abundance of halos in cosmological dark matter simulations to real observations of galaxies it has been shown that stars form most efficiently in $\simeq 10^{12} M_\odot$ halos (Moster et al. 2013; Behroozi et al. 2013a,b; Kravtsov et al. 2014), which is believed to occur because star formation is suppressed by stellar feedback and feedback from active galactic nuclei at lower and higher halo masses, respectively (Vogelsberger et al. 2013; Torrey et al. 2014; Schaye et al. 2014). An implication is that galaxies that reside in massive (e.g. $\sim 10^{14} M_\odot$ at $z = 0$) halos formed their stars earlier than galaxies that reside in $\sim 10^{12} M_\odot$ halos (at $z = 0$) because galaxies inside $10^{12} M_\odot$ halos at $z = 0$ are still forming stars with the highest possible efficiency. A consequence of this complicated relation between halo growth and star formation is the ‘downsizing’ scenario, in which the galaxies with the most-massive stellar components (e.g. $M_* \sim 10^{11} M_\odot$) at $z = 0$ formed their stars earlier than galaxies of more-moderate masses (e.g. $M_* \sim 10^{10} M_\odot$).

The aim of this article is to study properties of star-forming galaxies, especially the SFMS and the relation between halo growth and star formation, in the Illustris cosmological simulation. Section 2 describes Illustris, Section 3 analyses properties of the star formation main sequence, and Section 4 examines how the halo mass affects star formation in galaxies. In Section 5 we study star formation histories of galaxies, and we examine how the star formation history of a galaxy depends on its dark matter halo mass and black hole mass. We discuss our findings in Section 6 and summarise our conclusions in Section 7.

2 THE ILLUSTRIS SIMULATION

Illustris is a cosmological hydrodynamical simulation of a comoving volume of $(106.5\text{Mpc})^3$. The cosmological model used in Illustris is the Λ CDM cosmology with parameters from the WMAP7 data release (Hinshaw et al. 2013). Besides gravity and hydrodynamics, it includes treatments of gas cooling, star formation, and feedback from stellar winds, supernovae and AGN (see Vogelsberger et al. 2013, 2014a,b; Torrey et al. 2014). The Illustris simulation has previously been used to study a range of different galaxy properties, such as the evolution of damped Ly- α absorbers (Bird et al. 2014), the formation of elliptical and spiral galaxies (Vogelsberger et al. 2014b), the evolution of galaxy properties from high to low redshift (Genel et al. 2014), and the relation between the dark matter and stellar components in the faint outskirts of galaxies (Pillepich et al. 2014).

The initial conditions at a redshift of $z = 127$ include 1820^3 dark matter particles, 1820^3 gas cells, and 1820^3 Monte Carlo tracer particles (Genel et al. 2013). The gravitational softening length for the dark matter particles is 1420 comoving pc. The gravitational softening lengths of the gas cells depend on the cell size; they have a minimum value of 710 physical pc. Star particles have a softening length of 1420 comoving pc at $z \geq 1$, and at lower redshifts, the softening length is fixed to 710 physical pc. The mass of

¹ It is sometimes claimed that galaxies on the SFMS must not be undergoing mergers. This is a misconception: for most of the duration of mergers, the SFR is not elevated significantly by the interaction (e.g. Cox et al. 2008; Hopkins et al. 2010). Consequently, merging galaxies often lie on the SFMS (see fig. 11 of Hayward et al. 2012). Thus, it is important to not equate galaxies that lie above the SFMS with mergers. Instead, galaxies above the SFMS should be referred to as ‘starbursts’ (by definition), which may or may not be merger-induced. Galaxies on the SFMS should be considered ‘quiescently star-forming’, and such galaxies may still be involved in an ongoing merger.

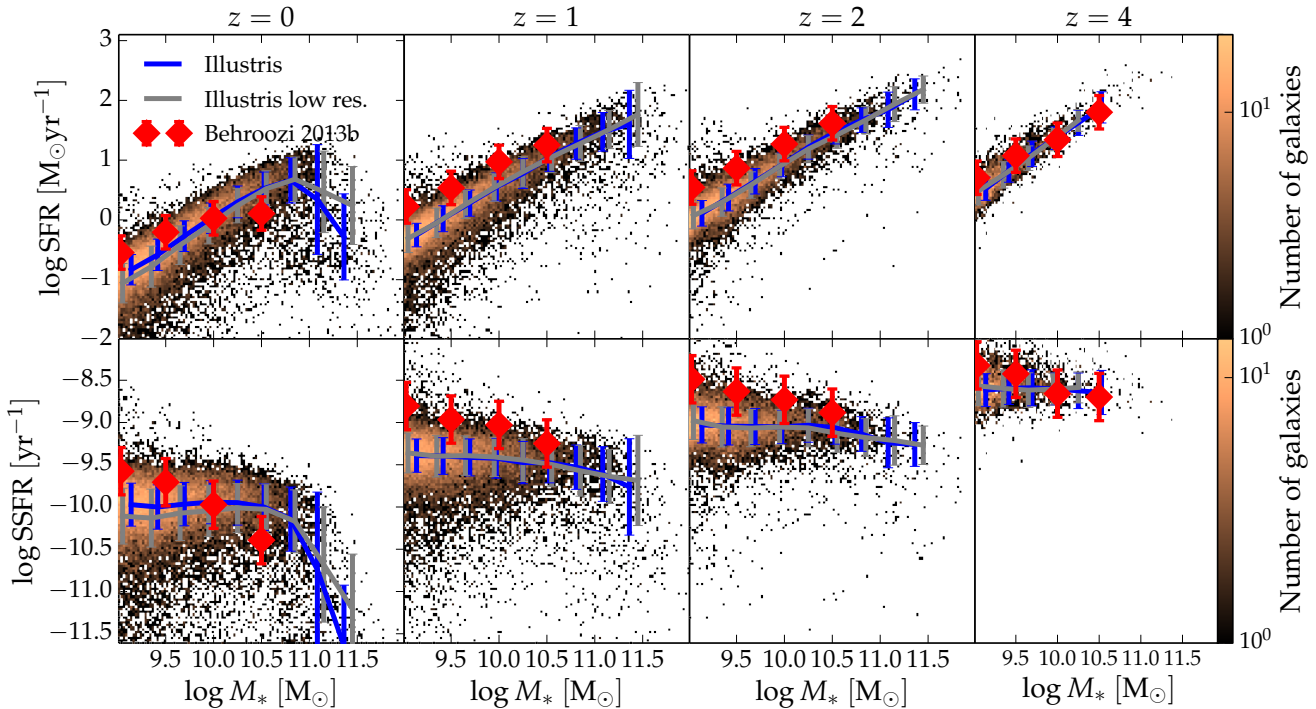


Figure 1. The star formation main sequence at $z = 0, 1, 2$ and 4 for the Illustris simulation (the two-dimensional histogram in the background). The upper panels show the median SFR, and the lower panels show the median SSFR. The simulation results are compared to the compilation of observations from Behroozi et al. (2013b), where the error bars indicate 68% confidence intervals for the inter-publication variance. The grey and blue error bars denote the 1σ errors estimated by fitting Gaussian functions to the SFR distributions of galaxies in narrow mass bins in the low-resolution and high-resolution versions of Illustris, respectively.

the dark matter particles is $6.26 \times 10^6 M_\odot$, and the gas cell target mass is $1.26 \times 10^6 M_\odot$. In this paper we will also study a simulation with lower resolution (a total of 3×910^3 dark matter, gas and tracer particles, implying 8 times worse mass resolution and two times poorer spatial resolution), but with the same physical galaxy formation model. We will refer to this simulation as the *Illustris low resolution run*.

The hydrodynamical calculations in Illustris are done with the AREPO code (Springel 2010), where the hydrodynamical forces are computed on a moving mesh built with a Voronoi tessellation. With a spatial resolution of $\simeq 1$ kpc there is no hope to resolve giant molecular clouds, where star formation takes place in the Universe. Instead a sub-resolution model is implemented (Springel & Hernquist 2003; Vogelsberger et al. 2013, 2014a), where unresolved physical processes such as the formation of molecular clouds, thermal instabilities, and supernova feedback are coarsely described with an effective equation of state. When a gas cell exceeds a hydrogen number density of $\rho_{\text{th}} = 0.13 \text{ cm}^{-3}$ it produces star particles stochastically on a density-dependent timescale of

$$t_*(\rho) = t_0^* \left(\frac{\rho}{\rho_{\text{th}}} \right)^{-1/2}, \quad (1)$$

where $t_0^* = 2.2$ Gyr. With the chosen values of ρ_{th} and t_0^* , galaxies obey the empirical Kennicutt-Schmidt relation between the gas surface density and the star formation rate per surface area of a galaxy (Kennicutt 1989). A star particle in this model represents an entire stellar population born with a Chabrier initial mass function (Chabrier 2003). During each timestep of the simulation, the amount of H, He, C, N, O, Ne, Mg, Si and Fe released by each stellar population is calculated and returned to the gas.

The formation of stars is accompanied by the release of kinetic winds from supernovae, which contribute to expelling the surrounding gas and to the chemical enrichment of the interstellar gas. The wind velocity is 3.7 times the one-dimensional velocity dispersion of the dark matter near the star forming region.

In friends-of-friends groups more massive than $1.7 \times 10^{10} M_\odot$ black holes are seeded, and a model of AGN feedback is included (Springel et al. 2005; Sijacki et al. 2007), where a quasar can be in a radio-quiet or radio-loud mode. In the latter mode, thermal energy is injected into the gas surrounding the black hole. Also included is a treatment of AGN radiative feedback, which heats the gas surrounding the AGN and changes its ionization state (see full description in Vogelsberger et al. 2013).

Also implemented are processes such as radiative cooling, chemical evolution, and an ultraviolet background. For a full description of the physical model of Illustris, see Vogelsberger et al. (2013) and Torrey et al. (2014).

3 THE STAR FORMATION MAIN SEQUENCE

A *star formation main sequence* (SFMS) that relates the star formation rate and the stellar mass of galaxies is recovered in Illustris; see Figure 1, which shows the relation at $z = 0, 1, 2$ and 4 . The SFMS is plotted in terms of both the SFR and specific SFR, $\text{SSFR} \equiv \text{SFR}/M_*$, versus M_* . The simulation is compared with the compilation of observations by Behroozi et al. (2013b, Table 8), who fit a relation to a large number of measurements from different authors and quantified the scatter in the observations of the SFMS from different publications. This scatter, which is denoted by the er-

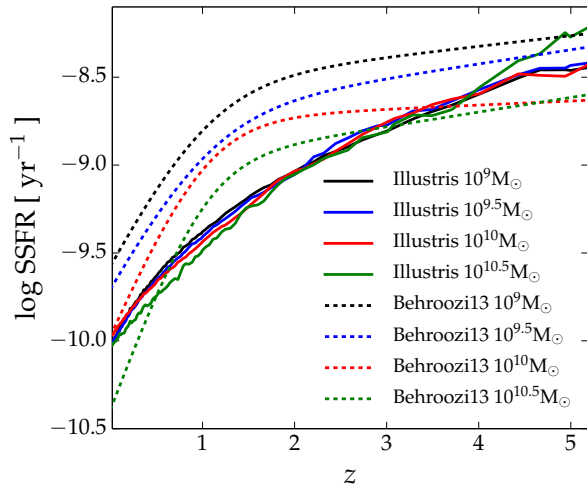


Figure 2. The median SSFR as function of redshift for galaxies with different stellar masses. At each redshift the SSFR of galaxies in the given stellar mass bin is computed. The dashed lines show the compilation of observations from Behroozi et al. (2013b). The different evolution of the SSFR from $z = 4$ to $z = 0$ is closely related to the too low normalisation of the star formation main sequence at $z = 1$ and $z = 2$ in Figure 1.

ror bars in Figure 1, quantifies the inter-publication variance of the SFMS and therefore accounts for the systematic error arising when measuring the SFMS with different methods. The normalisation in Illustris agrees with the observational constraints from Behroozi et al. (2013b) at $z = 0$. The figure also shows that the normalisation of the SFMS in Illustris is well converged above $M_* = 10^9 M_\odot$.

At $z = 4$, Illustris is also in excellent agreement with the observed relation. However, despite being in good agreement at $z = 0$ and $z = 4$, the normalisation of the SFMS is significantly lower than the observational constraints at intermediate redshifts of $z = 1$ and $z = 2$ (this has been previously noted and discussed for Illustris; see Genel et al. 2014). Several studies have previously pointed out discrepancies between the observed SFMS relation and galaxy formation models (e.g., Daddi et al. 2007; Davé 2008; Damen et al. 2009), especially at $z \simeq 2$. In Illustris, this problem takes only the form of reproducing the correct evolution of the main sequence at intermediate times between $z = 4$ and $z = 0$, whereas the simulated relations at these boundary epochs are consistent with observations.

The SSFR in Illustris becomes approximately independent of mass for $M_* < 10^{10.5} M_\odot$ (Figure 1, *lower panels*), which is a small but remarkable difference from the observations of Behroozi et al. (2013b), which indicate a declining SSFR as function of mass. Figure 2 shows the redshift evolution of the SSFR for galaxies with different stellar masses. The SSFR is here determined by calculating the normalisation of the SFMS in different stellar mass bins. Since the SSFR is independent of mass at fixed redshift in Illustris, the SSFRs of galaxies from different mass bins have the same redshift evolution. The fitting relations from Behroozi et al. (2013b) show a somewhat different evolution, partially because the SSFR is mass-dependent at fixed redshift. We note that the problem with reproducing the evolution of the SSFR (in Figure 2) is closely related to the problem of reproducing the normalisation of the SFMS at $z = 1$ and $z = 2$ (in Figure 1). Genel et al. (2014) also studied the redshift evolution of the SSFR in Illustris and found that the SSFR of galaxies is closely tied to the galaxies’ dark matter accretion rate.

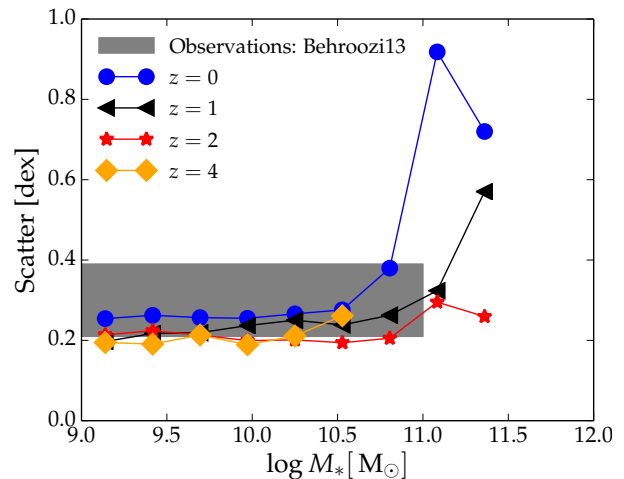


Figure 3. The scatter in the main sequence as function of mass for four different redshifts. The grey box shows the range of scatter in typical observations (from Behroozi et al. 2013b). Above $10^{11} M_\odot$ there are no reliable observational constraints for the scatter.

3.1 The scatter in the main sequence

The intrinsic scatter in the galaxy main sequence is predicted to be driven by the different gas accretion histories of different galaxies (see the analytical modelling of Dutton et al. 2010). Observations typically reveal a scatter of 0.21–0.39 dex (this reflects the range of values given in Table 9 in Behroozi et al. 2013b), but the measured scatter will of course depend on the exact selection criteria for the star-forming galaxies which form the main sequence (e.g. Whitaker et al. 2012) as well as on the uncertainties in SFR indicators.

To measure the scatter in the SFMS, we perform a Gaussian fit to the distributions of SFRs in different stellar mass bins. This method is similar to what is used in Rodighiero et al. (2011). In Figure 3, we show the scatter in the Illustris galaxies’ SFR values as function of stellar mass for four different redshifts. Below $10^{10.5} M_\odot$, the scatter is constant at 0.2–0.3 dex at each redshift, which is in excellent agreement with observational constraints. At the high-mass end ($M_* > 10^{10.5} M_\odot$), the scatter deviates from the value at lower masses because the galaxy main sequence is ill-defined at these high masses in Illustris (this is also seen in Figure 1).

3.2 Star formation above the main sequence relation

After having examined the behaviour of the main sequence relation and its scatter in the Illustris simulation, we will now look at starburst galaxies that lie significantly above the main sequence relation. In Figure 4 the fraction of stars formed in galaxies on and above the main sequence is computed at different redshifts. We define a galaxy to be on the main sequence relation if the SFR is within 2.5σ of the SFMS relation, which is the same criterion used in Rodighiero et al. (2011). For $M_* > 10^{10} M_\odot$ the fraction of stellar mass formed in galaxies above the SFMS relation is lower than the observational result reported by Rodighiero et al. (2011) at $1.5 < z < 2.5$. We also note that the fraction of star formation that occurs above the main sequence is consistent in the high- and low-resolution Illustris runs for $M_* > 10^{9.5} M_\odot$. In Section 6.2 we will further discuss the paucity of starbursts in Illustris.

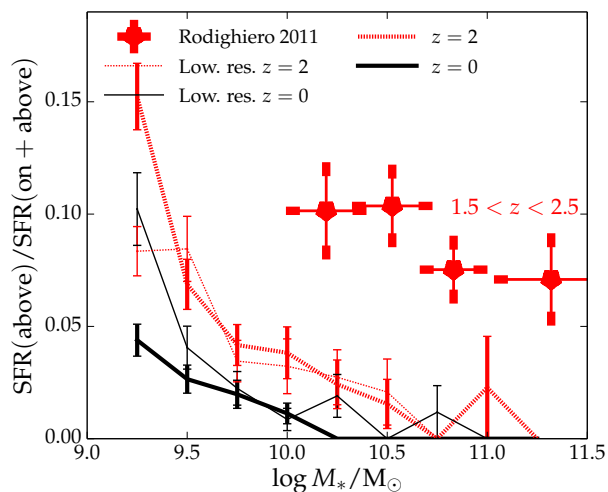


Figure 4. The fraction of stellar mass formed by galaxies 2.5σ or higher above the SFMS at $z = 0$ and $z = 2$. The thick and thin lines show the high- and low-resolution Illustris runs, respectively. The error bars indicate the contribution of Poisson noise. The simulated galaxy distribution is compared to the observational measurement at $1.5 < z < 2.5$ from Rodighiero et al. (2011).

3.3 The choice of SFR indicator

The SFR of a galaxy can be inferred using different diagnostics, such as the $H\alpha$ luminosity, the ultraviolet luminosity or the total infrared luminosity (Kennicutt & Evans 2012). Different diagnostics are sensitive to the past SFR in a galaxy smoothed over different timescales, so if a galaxy has a very rapidly changing SFR, different indicators will yield different SFR values. The timescale for which different indicators are sensitive can vary from tens to hundreds of megayears. A situation in which one has to be particularly careful to rely on such averaging is in the post-starburst phase of merging galaxies, where simulations show that the SFR inferred from the total infrared luminosity overestimates the actual SFR of a galaxy by as much as two orders of magnitude (Hayward et al. 2014).

In Figure 5 the scatter in the main sequence is shown for four different definitions of the SFR. First, the SFR is calculated from the instantaneous gas properties of galaxies, which we regard as the true SFR of the galaxies. We additionally calculate the mean SFR from the mass of stars formed in the last 50, 250 and 500 Myr in a galaxy. The scatter in the main sequence is essentially the same in the cases where the SFR is calculated from the gas or the stars formed during the last 50 Myr. For the case where the SFR is calculated from the mass of stars formed in the last 250 Myr, the scatter in the main sequence decreases by 0.03 dex at both $z = 0$ and $z = 2$, and when averaged over 500 Myr, the scatter decreases by 0.05 dex. It is not surprising that the scatter declines when increasing the time over which the SFR is averaged, since the SFHs of galaxies are more similar when variability on a timescale smaller than e.g. 500 Myr is smoothed out.

For actively star-forming galaxies, most of the widely used SFR indicators are sensitive to timescales smaller than 200 Myr (Kennicutt & Evans 2012). Thus, we conclude that the timescale over which the SFR indicator is sensitive is very unlikely to change the derived scatter in the main sequence relation for the physics model used in Illustris, for which star formation is less bursty than

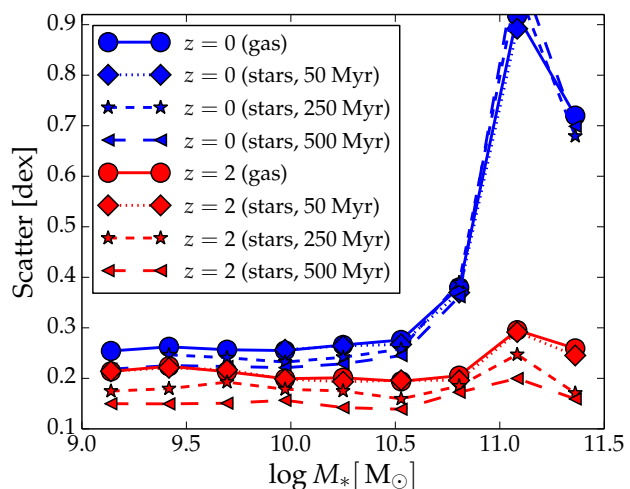


Figure 5. The main sequence scatter at $z = 0$ and $z = 2$ with the SFR measured in four different ways: from the instantaneous gas properties, and from the initial mass of the stars formed in the last 50, 250 and 500 Myr in the galaxies. When estimating the SFR from the stars formed in the last 500 Myr, the scatter is lower than in the other cases.

in reality. The systematic offsets between different indicators are likely of much greater importance.

It is possible that the role of the characteristic timescale of an SFR indicator will have an impact on the derived SFR for feedback models other than the one used in Illustris. Hopkins et al. (2013) and Governato et al. (2014), for example, present feedback models with typical variability timescales of 10–100 Myr. In Section 5 we further discuss the characteristic variability timescales of feedback models.

4 HALO MASS AND STAR FORMATION PROPERTIES OF GALAXIES

4.1 Halo and stellar masses of star-forming galaxies

Closely related to the main sequence of star forming galaxies is the cosmic comoving SFR density (SFRD). Assuming that all galaxies lie on the main sequence relation, the SFRD can be calculated as

$$\text{SFRD} = \int \text{SFR}_{\text{SFMS}}(M_*) \times \frac{dn}{dM_*} dM_*, \quad (2)$$

where n is the comoving number density of galaxies, M_* is the stellar mass, and $\text{SFR}_{\text{SFMS}}(M_*)$ is the main sequence relation. The SFRD is observed to peak at $z \simeq 2$ (Lilly et al. 1996; Madau et al. 1998; Hopkins 2004; Hopkins & Beacom 2006; Labbé et al. 2010; Cucciati et al. 2012), with the physical drivers of the evolution being the build-up of massive halos and the suppression of star formation by feedback from stellar winds and AGN (Schaye et al. 2010; Vogelsberger et al. 2013; Torrey et al. 2014).

Figure 6 shows how galaxies with different stellar masses and halo masses (M_{200}) contribute to the SFRD. This has been computed by summing the contribution to the SFRD from galaxies in equally spaced logarithmic mass-bins from $10^8 M_\odot$ to $10^{14.5} M_\odot$. Bins containing 7 or fewer galaxies are excluded from the plot in order to avoid bins with very high Poisson noise. The plot also shows

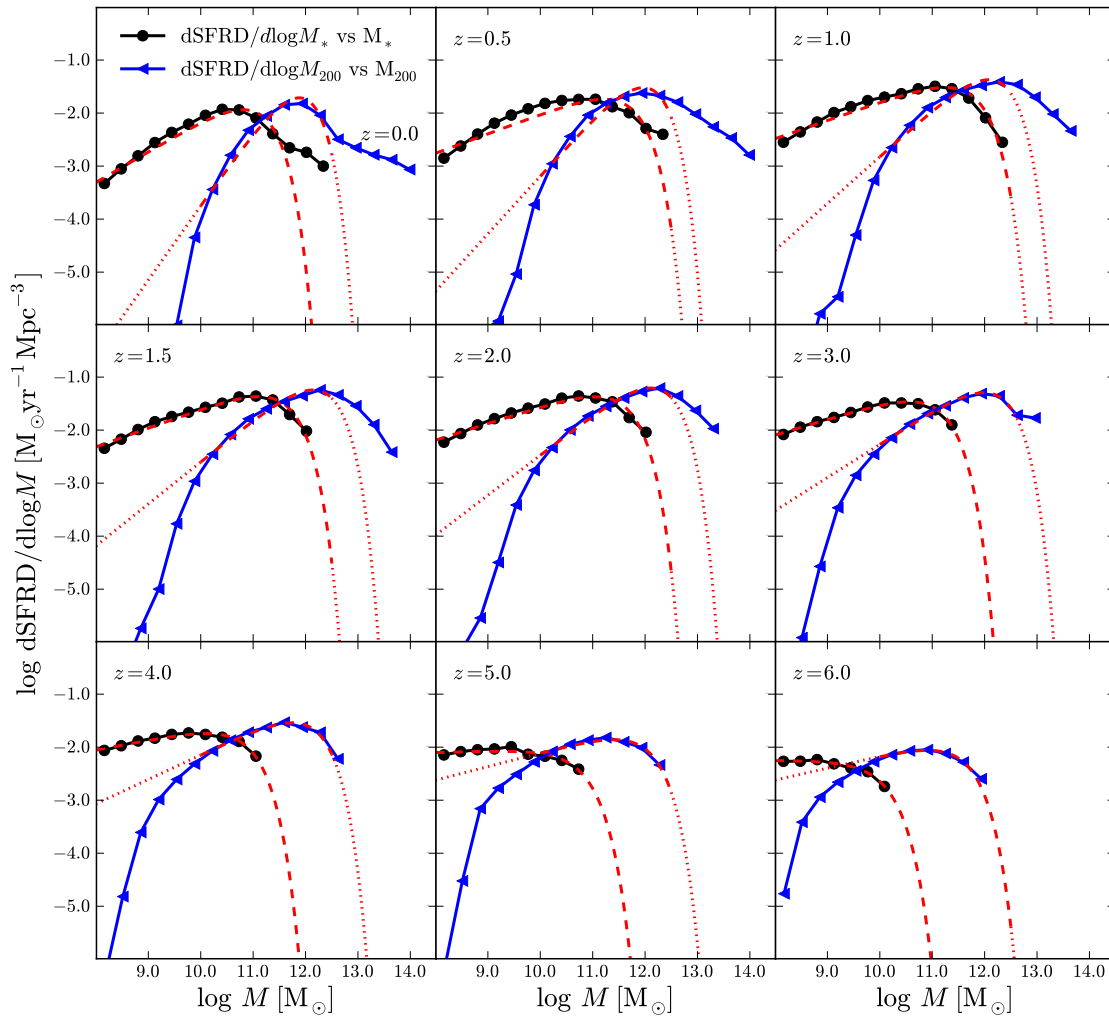


Figure 6. The contribution of halos with different stellar masses (black circles) and halo masses (blue triangles) to the total SFRD in the Universe at different redshifts. The red dashed lines are Schechter functions of the form of Eq. (3) fit to the simulation data (outside the fit range the extrapolated Schechter functions are dotted). The distributions evolve with redshift as halos and galaxies grow. This is also seen in Figure 7, where evolution of the peak mass is examined.

how Schechter functions of the form,

$$\text{SFRD}(M) \propto \left(\frac{M}{M_{\text{sch}}}\right)^{\alpha} \times \exp\left(-\frac{M}{M_{\text{sch}}}\right), \quad (3)$$

fit to the measurements, where M is either M_{200} or the stellar mass in a halo and M_{sch} and α are free fit parameters. For the fits in terms of halo mass, we exclude halos outside the range $10^{10} M_{\odot} < M_{200} < 10^{12.5} M_{\odot}$, since a Schechter function does not yield a good fit over the entire range of M_{200} -values of the halos. For fits in terms of stellar mass, all galaxies with $10^8 M_{\odot} < M_* < 10^{12.5} M_{\odot}$ are included. The actual distributions measured from the Illustris simulation are overall quite well described by the Schechter fits. This is consistent with the observations from Karim et al. (2011), where the distributions of $\text{dSFR}/\text{dlog } M_*$ are also well fit by a Schechter function for (at least) $M_* > 10^8 M_{\odot}$.

The peak masses of the distributions for $\text{dSFR}/\text{dlog } M_{200}$ and $\text{dSFR}/\text{dlog } M_*$ are plotted at different redshifts in Figure 7. At $z \lesssim 4$ the peaks in the distributions occur at $10^{11.5} < M_{200}/M_{\odot} < 10^{12.5}$ and $10^{10.0} < M_*/M_{\odot} < 10^{11.0}$. Illustris is therefore in agreement with the observations from Karim et al.

(2011), where $\text{dSFR}/\text{dlog } M_*$ peaks at $M_* \simeq 10^{10.5 \pm 0.2} M_{\odot}$ for $z \lesssim 2.5$. A large contribution of star formation from halos with $M_{200} = 10^{12} M_{\odot}$ is, e.g., also seen in the abundance matching analysis of Béthermin et al. (2013).

At $M_{200} \simeq 10^{12} M_{\odot}$, halos are most efficient in turning their baryons into stars. This is for example evident when examining M_*/M_{200} , which peaks around $M_{200} \simeq 10^{12} M_{\odot}$ (this relation is plotted for Illustris in Vogelsberger et al. 2014a and Genel et al. 2014). This is because AGN feedback suppresses the formation of stars in halos above this characteristic mass, and stellar winds are responsible for suppressing the formation of stars in lower mass halos. It is therefore not surprising that the peak in $\text{dSFR}/\text{dlog } M_*$ is present at $M_{200} \simeq 10^{12} M_{\odot}$ at $z \lesssim 4$. At $z \gtrsim 4$ there is a decline in the typical masses (both stellar and halo masses) at which stars are formed in Illustris, since halos and galaxies are less massive at high redshifts.

A feature that is also visible in Figure 7 is that the mass (both for halo and stellar mass) at which most of the star formation occurs declines from $z = 1$ to $z = 0$. This is consistent with the downsiz-

M_{200}/M_{\odot}	median(M_{200})/ M_{\odot}	min(M_{200})/median(M_{200})	max(M_{200})/median(M_{200})	N_{galaxies}
10^{11}	10^{11}	1.00	1.00	100
10^{12}	10^{12}	0.97	1.03	100
10^{13}	9.2×10^{12}	0.77	1.42	100

Table 1. Three samples with different halo masses, M_{200} . Each sample includes the 100 galaxies with masses closest to 10^{11} , 10^{12} and $10^{13} M_{\odot}$ at $z = 0$.

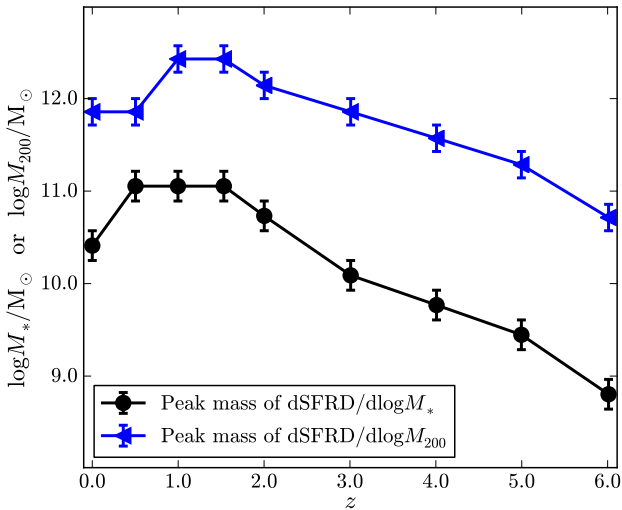


Figure 7. The redshift evolution of the peak stellar mass and halo mass for dSFR/dlog M_{200} and dSFR/dlog M_* , respectively, for the distributions in Figure 6. The peak mass (for both stars and halos) increases from $z = 6$ to $z \simeq 1 - 2$, after which it turns over. The error bars are set by the bin width of the histograms shown in Figure 6.

ing scenario, where the most-massive galaxies at $z = 0$ have older stellar populations than less-massive galaxies.

4.2 Build up of stellar components at different halo masses

To study how halo mass affects the average formation history of stars we create samples of halos with $M_{200} = 10^{11}, 10^{12}$ and $10^{13} M_{\odot}$. Each sample contains the 100 galaxies with halo masses closest to the mass that defines the samples. Table 1 summarizes the median, minimum and maximum halo mass in each sample. For each galaxy in each sample we compute the stellar mass growth history by calculating the amount of a galaxy’s stellar mass at $z = 0$ that was formed at different lookback times. For this analysis we include all stars within a halo at $z = 0$, including the stars residing in subhalos.

Figure 8 shows the median stellar growth history for each of the three samples. The galaxies ending up in the most-massive halos considered ($\sim 10^{13} M_{\odot}$) form their stars much earlier than the galaxies ending up in the least massive halos. This is most easily seen by comparing the times at which half of the stellar mass present at $z = 0$ is formed (shown as red circles in the figure). It is perhaps not surprising that very massive halos form their stars earlier than less massive ones, since halos of $10^{12} M_{\odot}$ contribute most to the global SFR in the Universe, as shown above. However, this trend runs counter to the formation time of the dark matter halos themselves, where the most massive halos form latest as a result of hierarchical structure growth.

We compare Illustris to the results from Behroozi et al. (2013b), where the stellar growth history is derived from the stel-

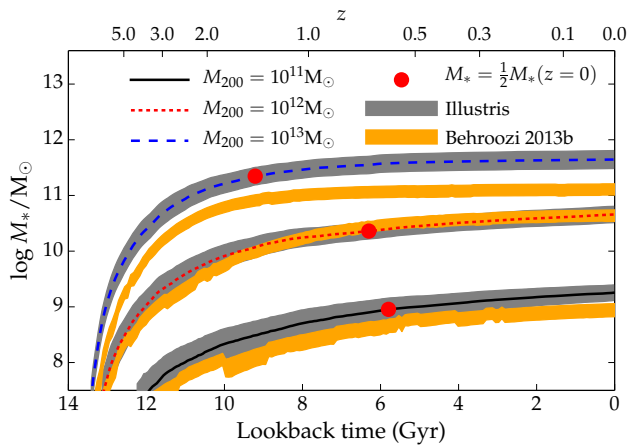


Figure 8. The fraction of the current stellar mass formed as function of lookback time for galaxies residing in halos with M_{200} -values of $10^{11} M_{\odot}$, $10^{12} M_{\odot}$ and $10^{13} M_{\odot}$ (see details about samples in Table 1). The grey shaded regions correspond to 1σ scatter in each mass range. The orange regions are the 1σ confidence intervals from the abundance matching of Behroozi et al. (2013b) for $M_{200}/M_{\odot} = 10^{11} M_{\odot}$, $10^{12} M_{\odot}$ and $10^{13} M_{\odot}$.

lar mass – halo mass relation ($M_*(M_h, z)$), which is determined by comparing dark matter merger trees with observations of the cosmic SFR, the specific SFR vs. M_* and stellar mass functions. For $10^{12} M_{\odot}$ halos, we find excellent agreement between Illustris and Behroozi et al. (2013b). At $10^{11} M_{\odot}$ and $10^{13} M_{\odot}$, Illustris predicts stellar components roughly 0.4 dex more massive than Behroozi et al. (2013b). This overproduction of stellar mass in halos of mass $\sim 10^{11} M_{\odot}$ and $\sim 10^{13} M_{\odot}$ is essentially independent of redshift. Genel et al. (2014) and Vogelsberger et al. (2014a) found similar deviations between the Illustris simulation and abundance matching results when analysing the high- and low-mass ends of the stellar mass function. Genel et al. (2014) regard these tensions as significant and suggest that more realistic feedback models could potentially help suppress the formation of too-massive stellar components in low- and high-mass galaxies.

5 STAR FORMATION HISTORIES OF GALAXIES

5.1 Outliers from the average star formation histories

An alternative to studying statistical properties of galaxies with different stellar masses is to analyse their individual star formation histories in more detail. To compute the star formation history (SFH) we select the stars ending up in a galaxy at $z = 0$, and then create a histogram of the initial mass of stars formed in 100 equally spaced bins in terms of lookback time. We include all stars that end up in the main stellar component of a galaxy (i.e. we exclude satellites) when calculating the SFH in this way. We do not distinguish between stars formed in-situ or ex-situ. We study galaxies in four different stellar mass ranges at $z = 0$. Three ranges are centered

M_*/M_\odot	median(M_*)/ M_\odot	min(M_*)/median(M_*)	max(M_*)/median(M_*)	N_{galaxies}
10^9	1.0×10^9	0.99	1.02	500
10^{10}	1.0×10^{10}	0.95	1.05	500
10^{11}	9.4×10^{10}	0.83	1.30	500
$> 1.57 \times 10^{11}$ (most massive)	2.6×10^{11}	0.60	12.70	500

Table 2. Four different samples of galaxies in different stellar-mass-ranges. The first three samples include the 500 galaxies with stellar masses (M_*) closest to 10^9 , 10^{10} and $10^{11} M_\odot$ at $z = 0$. The fourth range includes the 500 galaxies with the largest stellar masses at $z = 0$. The median, minimum and maximum stellar mass for each sample is also listed.

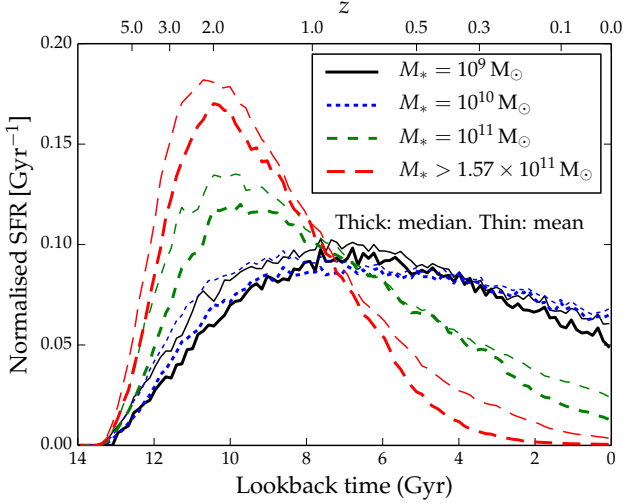


Figure 9. Mean and median (thin and thick lines, respectively) star formation histories of galaxies in the four different stellar mass ranges (see Table 2). The star formation rates are normalised so that $\int \text{SFR}(t) dt = 1$.

around $M_* = 10^9 M_\odot$, $M_* = 10^{10} M_\odot$ and $M_* = 10^{11} M_\odot$, with the widths of the different ranges chosen such that they include 500 galaxies each. We additionally create a range of the 500 galaxies with the most-massive stellar components. Basic properties of the different samples are summarised in Table 2.

The mean and median star formation histories of the galaxies in the different mass-ranges are shown in Figure 9. For the $10^{11} M_\odot$ range and the 500 most-massive galaxies the SFH peaks at $z \simeq 2$, and decreases at later epochs. These trends are qualitatively in good agreement with other studies of star formation histories of galaxies (e.g. Behroozi et al. 2013b; Simha et al. 2014). For the $10^9 M_\odot$ and $10^{10} M_\odot$ mass ranges, the peak is significantly broader, and it occurs at $z \simeq 1$. In general, the mean SFR is 10–20% larger than the median value, since the mean is more sensitive to extreme outliers with high SFRs.

Different galaxies experience a variety of gas accretion and merger histories, and they are therefore expected to exhibit diverse SFHs. We illustrate this in Figure 10, where we show for each mass range the SFR of the galaxies that form 50% of their stellar mass earliest or latest, compared to the average history of the corresponding sample. In all mass ranges, it is possible to find SFHs with early or late star formation. The galaxies with decidedly early star formation histories exhibit a similarly bursty epoch at a lookback time of $\simeq 10 - 13$ Gyr, and the galaxies with late star formation histories display a prominent star forming mode contributing at $z \lesssim 0.5$ and hardly any high-redshift star formation.

5.2 Modes of star formation in a principal component analysis

The relative similarity seen in Fig. 10 of the galaxies in the tails of the star formation history distribution, forming their stars extremely late or early, suggests that a more systematic study of the star formation modes in the Illustris galaxies is worthwhile. As a tool for statistically characterizing the star formation histories we have adopted a *principal component analysis* (PCA; inspired by Cohn & van de Voort 2014) where the SFH of a galaxy is seen as a vector in a N -dimensional space, where N is the number of bins used to characterize the SFH of a galaxy (we use $N = 100$). A key quantity in a PCA analysis is the average SFH of the galaxies in the sample,

$$\langle \text{SFR} \rangle(t_i) = \frac{1}{N_{\text{galaxies}}} \sum_{j=0}^{N_{\text{galaxies}}-1} \text{SFR}_j(t_i), \quad (4)$$

for $i = 0, \dots, N - 1$. We furthermore define the scatter matrix,

$$C_{mn} = \sum_{j=0}^{N_{\text{galaxies}}-1} [\text{SFR}_j(t_m) - \langle \text{SFR} \rangle(t_m)] [\text{SFR}_j(t_n) - \langle \text{SFR} \rangle(t_n)], \quad (5)$$

Of special interest are the eigenvectors of C_{mn} , which are called the *principal components* (PC_i , for $i = 0, \dots, N - 1$) and describe the deviations between the SFH of individual galaxies and the mean SFH of a sample. Principal components diagonalize the scatter matrix, implying that the scatter between different PC_i 's is uncorrelated. Conventionally the PCs are ordered in descending order by the contribution they make to the total variance. Often, the first components account for much of the variance, and the corresponding eigenvectors can be interpreted in physical terms. In our case they can serve the purpose of characterizing the most important ‘modes’ of the SFH.

In terms of the principal components, the SFH of a galaxy can be written as

$$\text{SFR} = \langle \text{SFR} \rangle + \sum_{i=0}^{N-1} q_i \times \text{PC}_i, \quad (6)$$

where q_i is the coefficient determining the strength of the contribution of PC_i for a specific galaxy. Since we have binned our SFHs in $N = 100$ bins we formally get 100 principal components, and for each of the 500 galaxies in each sample we obtain 100 coefficients q_i . The limited size of our galaxy set means that only the leading PC components are robust against the noise.

Figure 11 shows the mean SFH for the $M_* = 10^{10} M_\odot$ sample together with the three leading modes, PC_0 , PC_1 and PC_2 . The PC_0 -mode accounts for galaxies forming stars early or late, depending on whether the coefficient q_0 is positive or negative. PC_1 and PC_2 cross the zero-point two and three times, respectively, and they are therefore determining the more detailed evolution of the

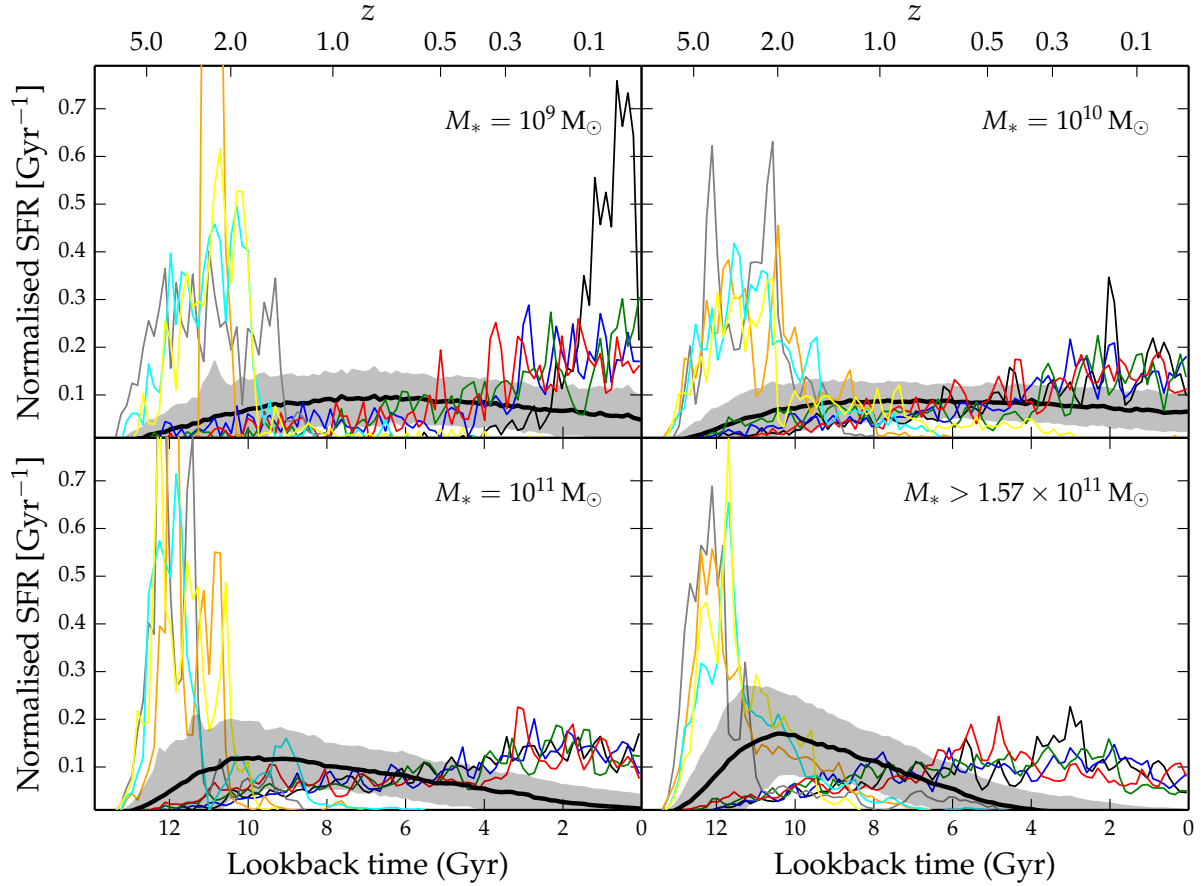


Figure 10. For each M_* -range, we have selected the four galaxies that form 50% of their stars earliest or latest (thin lines). The galaxies that form their stars early are shown in grey, orange, cyan and yellow, and the late galaxies are black, blue, green and red. The median profiles for each range are shown by the thick black lines, and the 68% confidence intervals are the grey shaded regions. The normalisation convention is $\int \text{SFR}(t) dt = 1$.

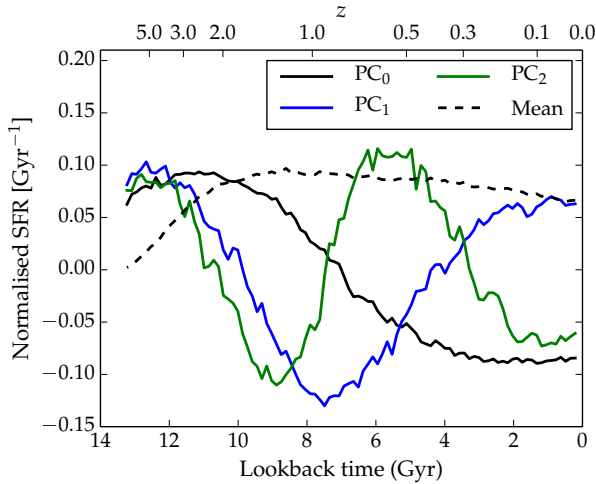


Figure 11. The mean SFR for the sample with $M_* = 10^{10} M_\odot$ (from Table 2) together with the first three principal components (PC_i for $i = 0, 1, 2$) describing the scatter around the mean. The normalisations of the principal components are arbitrary.

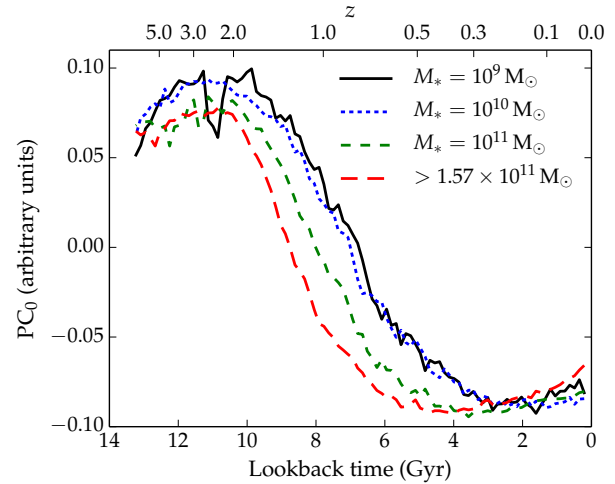


Figure 12. The zeroth principal component for the four different mass samples in Table 2. In all mass samples the PC_0 component is of similar shape and shows a positive contribution at a lookback time of 11 Gyr, and a negative contribution at lookback times smaller than $\simeq 7$ Gyr.

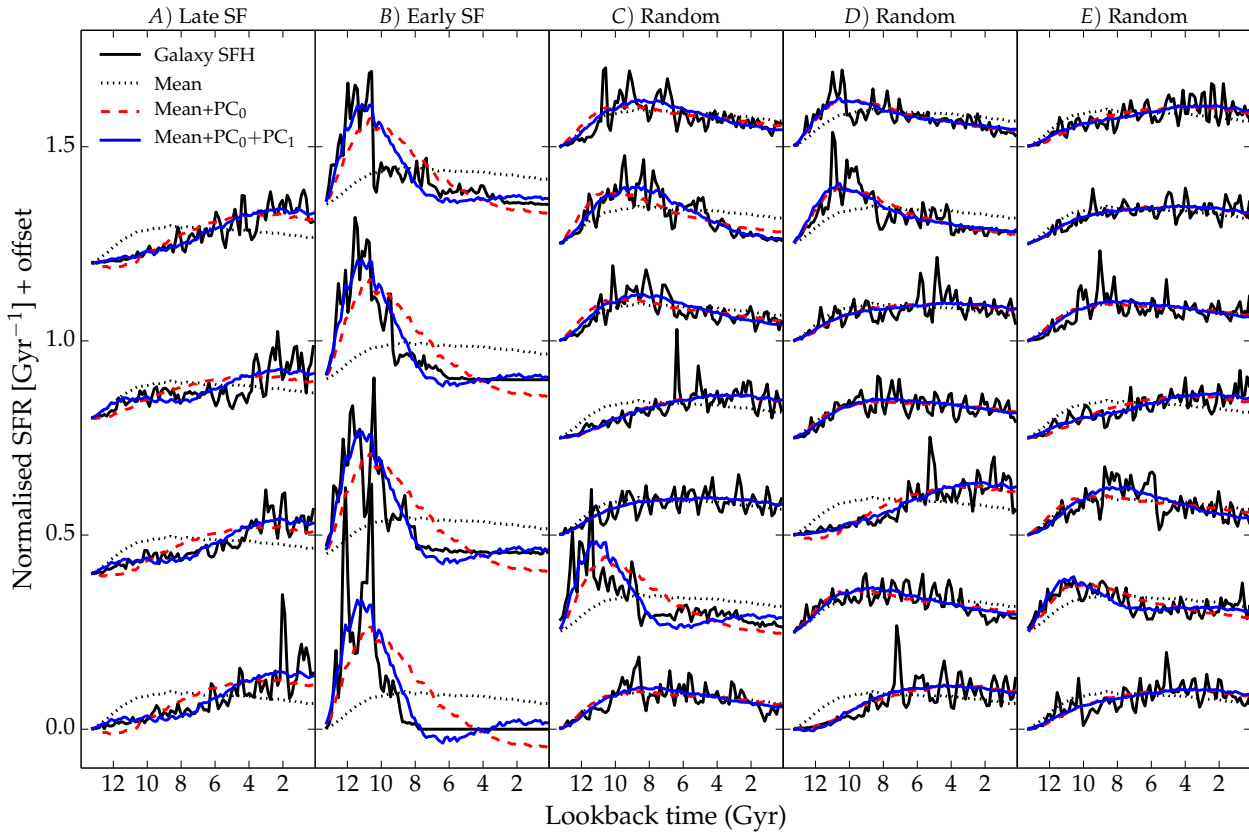


Figure 13. Star formation histories of individual galaxies (black lines) and the mean profile for the sample of galaxies with $M_* = 10^{10} M_\odot$ (grey dashed lines). Also shown are profiles including the contribution from the zeroth principal component (red dashed line) and components 0 and 1 (blue line). Panels A and B show 8 galaxies that form their stars late and early, respectively (the same profiles are shown in Figure 10). Panels C, D and E show 21 randomly selected galaxies from the sample with $M_* = 10^{10} M_\odot$.

SFH. In general, PC_i crosses the zero-point $i + 1$ times, and therefore is associated with a physical timescale of order $t_H/(i + 1)$, where $t_H = 13.7$ Gyr is the Hubble time.

For all the four mass samples from Table 2, the PC_0 is plotted in Figure 12. They all appear similar and have the feature that a positive q_0 -value describes a galaxy forming stars earlier than the mean of the sample. The only remarkable difference between the PC_0 eigenvectors from the different samples is that the lookback time where the change from positive to negative contributions occurs shifts to higher values for the more massive galaxies. The trend that massive galaxies have earlier bursty epochs than less massive galaxies is therefore both reflected by the mean star formation history and a 0th principal component that peaks at higher redshift.

Figure 13 compares the actual SFHs for a selection of galaxies to the mean SFH of the $M_* = 10^{10} M_\odot$ sample, and the SFHs reconstructed by including only PC_0 and by including both PC_0 and PC_1 . By including PC_0 it is possible to capture whether a galaxy forms its stars early or late. Including the PC_1 mode as well gives of course a better fit to the actual SFH of the galaxies. Components 0 and 1 account for 33% and 10% of the total scatter in the sample. These percentages indicate that while a given galaxy's SFH can already be described reasonably well by just PC_0 and PC_1 , variability on timescales much shorter than described by them needs to be considered for an accurate description.

We note that it could potentially be useful to construct a family of SFHs based on a combination of the mean SFH for the Il-

lustris galaxies and one or more of the principal components from the PCA analysis. An attractive property of a model based on the mean SFH and the leading principal component would be that it could describe a realistic SFH of a galaxy with only one free parameter (the relative contribution of the mean SFH and the leading principal component). Such a model would be more physically motivated than e.g. single-burst models or τ -models, which are often used when fitting spectral energy distributions of galaxies. In future work we will construct such a model and show how it can be used for fitting spectral energy distributions. Such an approach could yield significant advantages because the accuracy and robustness of spectral energy distribution modelling can be very sensitive to the assumed SFH (e.g. Michałowski et al. 2012, 2014; C. Hayward & D. Smith, submitted; P. Torrey et al., submitted).

5.3 Assessing the SFH variability timescale

As each principal component has an associated timescale, the PCA analysis may also be used to characterize variability of the star formation histories, which in turn is influenced by the adopted physical model for feedback processes and the ISM. In Figure 14, we show the cumulative fraction of the variance accounted for as a function of the number of principal components included. The two most-massive samples behave similarly for the low and high resolution run. For the two low mass bins the difference between the low and high resolution run is larger. To quantitatively measure how

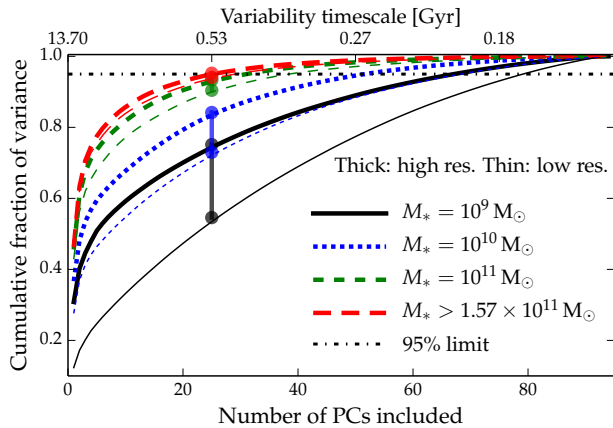


Figure 14. The cumulative fraction of the total variance in the star formation histories accounted for as a function of the number of principal components that are included. The thick lines show the full resolution run and the thin lines show the low resolution run. The vertical lines (connected by circles) measure how well-converged the variability timescale is for the different mass-ranges.

well-converged the cumulative fractions in Figure 14 are, we use the difference in the fraction of the scatter accounted for by the 25 first components in the low and high resolution run. For the various bins the differences are 21%, 11%, 3% and 1% (from lowest to highest mass). The two most-massive ranges are therefore well-converged, unlike the two least-massive ranges, where some of the scatter comes from Poisson noise. This is also consistent with Figure 9, where the mean and median star formation history of the low-massive range seem to be more affected by noise the most-massive range.

The timescale at which 95% of the scatter is accounted for is 500 Myr in the two most-massive bins, and for the other mass-ranges this timescale is smaller, which might be a consequence of the contribution of Poisson noise being more important in the low-massive galaxies, where there are fewer star particles per time bin. Based on the variability timescale of the most-massive range, the characteristic timescale for fluctuations in the galactic star formation for the ISM model adopted in Illustris has characteristic timescale of 500 Myr. In Section 3.3 we saw that the scatter in the SFMS decreased significantly (by 0.05 dex), when the SFH was smoothed on this timescale, and that the decrease in the scatter was more moderate when smoothing over shorter timescales.

We note that there exist other simulation feedback models which show variability timescales an order of magnitude lower than Illustris. Hopkins et al. (2013), for example, include a treatment of radiative feedback from young stars and more localized supernova feedback in giant molecular clouds. Another model with a short variability timescale is Governato et al. (2014), where this is achieved through a high-star formation threshold and delayed radiative cooling. Interestingly, variability itself could be used as an important constraint of feedback models, although the fact that highly variable feedback models will induce differences between SFR indicators may make this complicated in practice.

5.4 Relations between the SFH main mode and galaxy properties

We have previously shown that the q_0 -value of the PCA-decomposed star formation history of a galaxy captures whether

its stellar population forms early or late. We therefore expect correlations between q_0 and other quantities sensitive to the age of stellar populations. Figure 15 shows how q_0 for the different galaxy mass bins relates to the lookback time when half of the stellar mass is formed (T_{50}), the $g-r$ colour at $z=0$, the black hole mass at $z=0$, and the dark matter mass (friends-of-friends) at $z=0$. q_0 correlates strongly with T_{50} , which is in agreement with the star formation histories in Figure 13. There is an offset between the normalisation of this correlation between the different samples. This is partially because the most-massive galaxies form their stars before the least massive galaxies (see also Figure 9).

The correlation between q_0 and $g-r$ is also expected, since old stellar populations are expected to be redder than younger stellar populations. In all the samples there is a bimodality in the $g-r$ colour, which splits the galaxies into red galaxies (with high values of $g-r$) with large q_0 -values and blue galaxies (low values of $g-r$) with lower q_0 -values. The division between the blue and red galaxy populations is seen most clearly for the $M_* = 10^{11} M_\odot$ galaxies, where the red galaxies have $g-r \gtrsim 0.65$. For the sample containing the most-massive galaxies there is a larger fraction of red galaxies than for the samples of less massive galaxies, where the blue population dominates.

The presence of a red and blue population of galaxies that form their stars late and early, respectively, is consistent with the *red and blue cloud*, which are connected through the *green valley*, established from observations of galaxies (e.g. Strateva et al. 2001; Faber et al. 2007; Bowler et al. 2014; Schawinski et al. 2014). Galaxies in the blue cloud are known to be actively star-forming, whereas the red cloud consists of passive galaxies that are most likely quenched by feedback processes. In Illustris, there is a correlation between the star formation history and the black hole mass at $z=0$ for the three most-massive bins (*lower left panel*, Figure 15), which suggests that the galaxies that form their stars early are quenched by AGN feedback, although other interpretations of the correlation cannot be ruled out by the analysis presented here. For the $10^9 M_\odot$ galaxies, such a trend is not evident in the simulation, which is expected because the black hole feedback models in Illustris do not significantly affect galaxies in this mass range.

The panel that shows the dark matter halo mass, M_{halo} , at $z=0$ versus q_0 reveals that these two variables are correlated for the samples with the two highest stellar masses. Furthermore, galaxies that form their stars late (low q_0) have halo masses that are close to $10^{12} M_\odot$, whereas galaxies that form stars early have higher halo masses. This is expected within the framework in which stars are most likely to form in halos of mass $10^{12} M_\odot$. For the samples with $M_* = 10^9 M_\odot$ and $10^{10} M_\odot$ a weak anti-correlation between q_0 and M_{halo} is present. The anti-correlation most likely arises because a halo mass of $10^{12} M_\odot$ is never reached for these galaxies, so they form stars most efficiently at low redshift, when the dark matter halo mass is as close as possible to $10^{12} M_\odot$.

6 DISCUSSION

6.1 The normalisation of the star formation main sequence

In Section 3, we demonstrated that in Illustris, star-forming galaxies exhibit a tight, approximately linear correlation between the SFR and stellar mass, as is observed for real galaxies. Although the normalisation agrees well with observations at $z=0$ and $z=4$, the normalisation in Illustris is less than that observed for intermediate redshifts $z \sim 1-2$. A similar problem of underpredicting

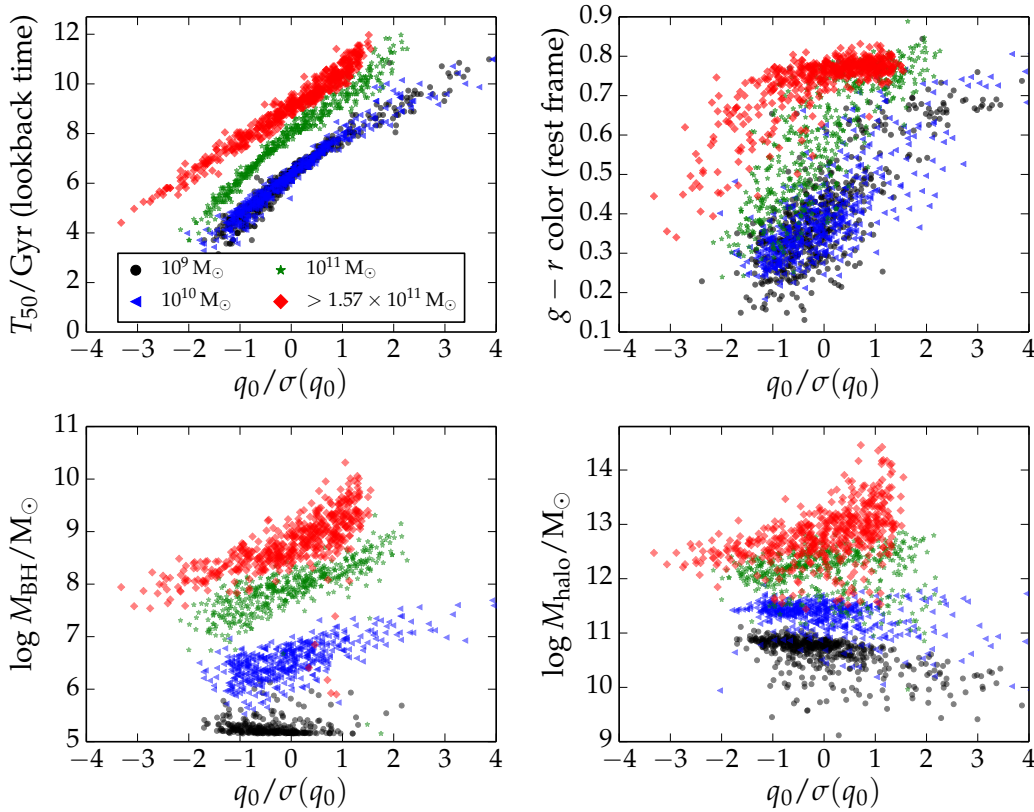


Figure 15. The dependence of various galaxy properties on the coefficient describing the contribution from the zeroth principal component (q_0) for each galaxy in the samples with stellar masses of $M_*/M_\odot = 10^9, 10^{10}, 10^{11}$, as well as for the 500 most-massive galaxies. The *upper left panel* shows that the lookback time at which 50% of the stars in a galaxy is formed (T_{50}) correlates strongly with q_0 . There also exists correlations with the $g-r$ colour (*upper right panel*), and the black hole mass at $z=0$ (*lower left panel*). For the two most-massive stellar mass samples, q_0 correlates with the dark matter halo mass. For the two samples with the least-massive galaxies, an anti-correlation is observed (*lower right panel*). q_0 is normalised by the standard deviation of this parameter for the 500 galaxies in each sample.

the normalisation of the main sequence relation at $z \simeq 2$ has previously been noted by several authors (e.g., Daddi et al. 2007; Davé 2008; Damen et al. 2009), and it appears to be a generic problem for cosmological hydrodynamical simulations and semi-analytical models. Thus, it is worthwhile to consider potential solutions to this problem and discuss whether it is indeed a serious problem.

6.1.1 Potential theoretical solutions

In Illustris and other cosmological hydrodynamical simulations, the SFR-stellar mass relation is a result of the correlation of gas inflow and outflow rates with halo mass (e.g. Davé et al. 2011, 2012; Dekel et al. 2013). Thus, inaccurate gas net accretion rates would lead to an incorrect normalisation of the SFR-stellar mass relation. Damen et al. (2009) compared the growth rate of galaxies in observations with semi-analytical models (Guo & White 2008) and argued that a time-varying IMF cannot resolve the issue of too low normalisations at $1 \lesssim z \lesssim 2$. Instead, Damen et al. suggest that the discrepancy may be due to the simplified schemes for gas accretion used in semi-analytical models. Mitchell et al. (2014) identified the same problem of a too low normalisation of the main sequence at $z=2$ in semi-analytical models. They showed that a modification of the timescale over which gas ejected by feedback is reincorporated into galaxies can help to fix this problem for galaxies with $M_* \lesssim 10^{10} M_\odot$ (a modification of the reincorporation timescale

was also studied by Henriques et al. 2013), but it cannot solve the problem for more-massive galaxies.

Concerns regarding gas inflow rates are less applicable to the Illustris simulation than to semi-analytical models because in Illustris gas accretion is explicitly treated using an accurate hydrodynamics algorithm (e.g. Sijacki et al. 2012; Vogelsberger et al. 2012; Kereš et al. 2012; Bauer & Springel 2012). Still, it is possible that the gas cooling rates in Illustris are systematically offset. For example, if the phase structure or metal content of the hot halo gas is incorrect, gas inflow rates could end up being inaccurate (Nelson et al. 2013; Hayward et al. 2014).

Outflows are also important for setting the normalisation of the SFR-stellar mass relation, but they must still be treated with sub-resolution models even in state-of-the-art large-volume cosmological hydrodynamical simulations. One can easily imagine altering the normalisation of the SFR-stellar mass relation by e.g. modifying the mass-loading factor of stellar winds. However, the parameters of the sub-resolution feedback models used in Illustris were determined by requiring the simulation to match observations such as the $z=0$ stellar mass function. Thus far, attempts to tune the parameters to reconcile the discrepancy with which we are concerned here without breaking these constraints were unsuccessful (Torrey et al. 2014). Nevertheless, this does not preclude the possibility of solving the discrepancy through the use of more sophisticated feedback models.

6.2 The paucity of starbursts in Illustris

The small number of strong starbursts (i.e. galaxies that lie significantly above the star formation main sequence) identified in Illustris is another discrepancy in addition to the disagreement in the normalisation of the SFR-stellar mass relation discussed above. As shown in Fig. 4, at all redshifts considered, 2.5σ outliers from the SFR-stellar mass relation contribute at most a few per cent of the total SFR density in massive galaxies ($M_* \gtrsim 10^{10} M_\odot$), and this contribution is a factor of at least a few less than what is inferred from observations. Furthermore, by combining scalings derived from idealised merger simulations with a semi-empirical model, Hopkins et al. (2010) estimated that at all redshifts, merger-induced starbursts account for $\sim 5 - 10$ per cent of the SFR density of the Universe, which is also at odds with the Illustris results.

One possible reason for the relative shortage of starbursts in Illustris is its kiloparsec-scale spatial resolution. Although the comparison of the low- and high-resolution runs presented in Figure 4 suggests that the fraction of starbursts is converged, it is possible that this conclusion will change if the resolution is increased significantly, as is often done using zoom-in simulations of galaxies (e.g.; Guedes et al. 2011; Marinacci et al. 2014). It is for example possible that the spatial resolution in both the high- and low-resolution Illustris runs is insufficient to resolve the tidal torques that drive starbursts in mergers. Indeed, the compact sizes (of order 100 pc) of the starbursting regions in local ULIRGs (e.g. Sakamoto et al. 2008; Engel et al. 2011) support this interpretation. Furthermore, examination of the individual star formation histories presented in Fig. 10 indicates that the galaxies' star formation was burstier at high redshift ($z \gtrsim 2$). Because a fixed comoving softening yields finer resolution at higher redshifts, this observation may also indicate that resolution is the reason for the lack of starbursts in Illustris.

The relatively stiff equation of state of the Springel & Hernquist (2003) sub-resolution ISM model may also serve to suppress starbursts in Illustris. However, in higher-resolution idealised merger simulations that employed the same ISM model, SFR elevations of an order of magnitude or more have been found (e.g. Cox et al. 2008; Hayward et al. 2011, 2014; Torrey et al. 2012). Furthermore, the resulting SFR elevations are sufficient to match the observed interaction induced SFRs of close-pair galaxies in SDSS (Scudder et al. 2012; Patton et al. 2013). We note however that galaxy merger simulations with much softer equations of state show still stronger (albeit shorter) SFR increases (e.g. Mihos & Hernquist 1996). Also, the elevation depends sensitively on the mass ratio and orbital parameters of the merger (e.g. Di Matteo et al. 2007, 2008; Cox et al. 2008). Thus, the sub-resolution ISM model may contribute to the suppression of merger-driven starbursts in Illustris but is unlikely to be the sole reason. But mergers are not the only mechanism that can drive starbursts: it has been suggested that violent disk instability is also an important channel for driving starbursts (e.g. Dekel et al. 2009; Ceverino et al. 2010; Cacciato et al. 2012; Porter et al. 2014). Such events may be suppressed in Illustris because of the sub-resolution ISM model.

Finally, it is possible that the IR luminosity-inferred star formation rates of extreme outliers from the main sequence are overestimates of the true SFR. For highly obscured galaxies, at the peak of the starburst, simulations suggest that older stellar populations (Hayward et al. 2014) and obscured AGN (L. Rosenthal et al., in preparation) may contribute to the IR luminosity and thus cause the SFR to be overestimated by a factor of a few. These effects are almost certainly not significant for the bulk of the star-forming galaxy

population and thus should not affect the normalization of the SFR-stellar mass relation, but, if they are relevant for any real galaxies, it will likely be those galaxies that are well above the galaxy main sequence. Consequently, these effects may explain the tension between observations and Illustris demonstrated in Section 3.2.

7 CONCLUSIONS

In this work, we have examined the star formation main sequence and individual star formation histories of galaxies in the Illustris simulation. Our main findings can be summarized as follows:

- The normalisation of the star formation main sequence is consistent with the observations at $z = 0$ and $z = 4$. At intermediate redshifts, $z \sim 2$, the normalisation is significantly lower than reported in observations. There is also a slight tension between the slope of the star formation main sequence for low-mass galaxies, for which Illustris predicts an approximately mass-independent specific SFR, whereas observations indicate that the specific SFR is a decreasing function of stellar mass. We speculate that more-sophisticated feedback models are required in order to properly recover the observed slope and normalisation of the SFMS.
- The highest star formation efficiency is found in halos with masses of $10^{12} M_\odot$, and the largest contribution to the star formation rate density comes from galaxies in halos with masses of $10^{11.5} - 10^{12.5} M_\odot$ at $z \lesssim 4$. At higher redshift, the dominant contribution originates in less-massive halos because of the declining abundance of halos with high masses. The stellar masses of the galaxies contributing most strongly to the global star formation rate density lie in the range $10^{10} - 10^{11} M_\odot$, which is in agreement with observational constraints on this peak mass. Another result is that galaxies with stellar masses above $\simeq 10^{11} M_\odot$ that reside in $\sim 10^{12} M_\odot$ halos form their stars later than galaxies in more-massive halos. This is a consequence of star formation being most efficient in $\sim 10^{12} M_\odot$ halos.
- We have studied the dominant modes and the time variability of individual star formation histories with a principal component analysis, finding that the characteristic timescale of star formation fluctuations in the simulation is 500 Myr. Another result of this principal component analysis is that many features of a galaxy's star formation history can be described by the leading principal component. This leads us to suggest that star formation histories based on one or several principal components can be useful when fitting the spectral energy distribution of observed galaxies.
- Compared to observations, there is a paucity of strong starbursts in Illustris, as evidenced by the small number of galaxies that lie significantly above the star formation main sequence. This is likely caused in part by a lack of spatial resolution in the cosmological simulation, but it may also reflect the relatively stiff equation of state model used in Illustris' subgrid model for the regulation of star formation in the ISM.

In future cosmological simulations of galaxy formation, the relative frequency of starbursts may well turn out to be an important constraint that informs about adequate models for the ISM. In Illustris, starbursts are presumably damped in intensity and stretched in time by the stiff ISM model, without much affecting the stellar mass and the structural properties of merger remnants. If a significant number of starbursts are triggered by disk instabilities, which are suppressed by the ISM model used in Illustris, the resulting discrepancies could potentially be more significant. Refined simulation models will be necessary to clarify this question.

ACKNOWLEDGMENTS

We thank Sune Toft, Peter Behroozi, Nicholas Lee and David Sanders for useful discussions. The Dark Cosmology Centre is funded by the Danish National Research Foundation. CCH is grateful to the Klaus Tschira Foundation and the Gordon and Betty Moore Foundation for financial support. VS acknowledges support by the European Research Council under ERC-StG EXAGAL-308037.

REFERENCES

- Atek H., et al., 2014, arXiv:1406.4132
 Bauer A., Springel V., 2012, MNRAS, 423, 2558
 Behroozi P. S., Wechsler R. H., Conroy C., 2013a, ApJ, 762, L31
 Behroozi P. S., Wechsler R. H., Conroy C., 2013b, ApJ, 770, 57
 Béthermin M., Daddi E., Magdis G., Sargent M. T., Hezaveh Y., Elbaz D., Le Borgne D., Mullaney J., Pannella M., Buat V., Charmandaris V., Lagache G., Scott D., 2012, ApJ, 757, L23
 Béthermin M., Wang L., Doré O., Lagache G., Sargent M., Daddi E., Cousin M., Aussel H., 2013, A&A, 557, A66
 Bird S., Vogelsberger M., Haehnelt M., Sijacki D., Genel S., Torrey P., Springel V., Hernquist L., 2014, arXiv:1405.3994
 Bowler R. A. A., et al., 2014, MNRAS, 440, 2810
 Brinchmann J., Charlot S., White S. D. M., Tremonti C., Kauffmann G., Heckman T., Brinkmann J., 2004, MNRAS, 351, 1151
 Cacciato M., Dekel A., Genel S., 2012, MNRAS, 421, 818
 Cemile Marsan Z., et al., 2014, arXiv:1406.0002
 Ceverino D., Dekel A., Bournaud F., 2010, MNRAS, 404, 2151
 Chabrier G., 2003, PASP, 115, 763
 Cohn J. D., van de Voort F., 2014, arXiv:1406.2967
 Cox T. J., Jonsson P., Somerville R. S., Primack J. R., Dekel A., 2008, MNRAS, 384, 386
 Cucciati O., et al., 2012, A&A, 539, A31
 Daddi E., et al., 2007, ApJ, 670, 156
 Daddi E., et al., 2010, ApJ, 714, L118
 Damen M., Förster Schreiber N. M., Franx M., Labbé I., Toft S., van Dokkum P. G., Wuyts S., 2009, ApJ, 705, 617
 Davé R., 2008, MNRAS, 385, 147
 Davé R., Finlator K., Oppenheimer B. D., 2012, MNRAS, 421, 98
 Davé R., Oppenheimer B. D., Finlator K., 2011, MNRAS, 415, 11
 Dekel A., Sari R., Ceverino D., 2009, ApJ, 703, 785
 Dekel A., Zolotov A., Tweed D., Cacciato M., Ceverino D., Primack J. R., 2013, MNRAS, 435, 999
 Di Matteo P., Bournaud F., Martig M., Combes F., Melchior A.-L., Semelin B., 2008, A&A, 492, 31
 Di Matteo P., Combes F., Melchior A.-L., Semelin B., 2007, A&A, 468, 61
 Diemand J., Kuhlen M., Madau P., Zemp M., Moore B., Potter D., Stadel J., 2008, Nature, 454, 735
 Dressler A., 1980, ApJ, 236, 351
 Dutton A. A., van den Bosch F. C., Dekel A., 2010, MNRAS, 405, 1690
 Elbaz D., et al., 2011, A&A, 533, A119
 Engel H., Davies R. I., Genzel R., Tacconi L. J., Sturm E., Downes D., 2011, ApJ, 729, 58
 Faber S. M., et al., 2007, ApJ, 665, 265
 Faber S. M., Jackson R. E., 1976, ApJ, 204, 668
 Genel S., et al., 2014, arXiv:1405.3749
 Genel S., Vogelsberger M., Nelson D., Sijacki D., Springel V., Hernquist L., 2013, MNRAS, 435, 1426
 Genzel R., et al., 2010, MNRAS, 407, 2091
 Governato F., et al., 2014, arXiv:1407.0022
 Guedes J., Callegari S., Madau P., Mayer L., 2011, ApJ, 742, 76
 Guo Q., White S. D. M., 2008, MNRAS, 384, 2
 Hayward C. C., et al., 2014, arXiv:1402.0006
 Hayward C. C., Jonsson P., Kereš D., Magnelli B., Hernquist L., Cox T. J., 2012, MNRAS, 424, 951
 Hayward C. C., Kereš D., Jonsson P., Narayanan D., Cox T. J., Hernquist L., 2011, ApJ, 743, 159
 Hayward C. C., Torrey P., Springel V., Hernquist L., Vogelsberger M., 2014, MNRAS, 442, 1992
 Henriques B. M. B., White S. D. M., Thomas P. A., Angulo R. E., Guo Q., Lemson G., Springel V., 2013, MNRAS, 431, 3373
 Hinshaw G., et al., 2013, ApJS, 208, 19
 Hopkins A. M., 2004, ApJ, 615, 209
 Hopkins A. M., Beacom J. F., 2006, ApJ, 651, 142
 Hopkins P. F., Keres D., Onorbe J., Faucher-Giguere C.-A., Quataert E., Murray N., Bullock J. S., 2013, arXiv:1311.2073
 Hopkins P. F., Younger J. D., Hayward C. C., Narayanan D., Hernquist L., 2010, MNRAS, 402, 1693
 Hubble E. P., 1926, ApJ, 64, 321
 Karim A., et al., 2011, ApJ, 730, 61
 Kennicutt R. C., Evans N. J., 2012, ARA&A, 50, 531
 Kennicutt Jr. R. C., 1989, ApJ, 344, 685
 Kennicutt Jr. R. C., 1998, ApJ, 498, 541
 Kereš D., Vogelsberger M., Sijacki D., Springel V., Hernquist L., 2012, MNRAS, 425, 2027
 Klypin A. A., Trujillo-Gomez S., Primack J., 2011, ApJ, 740, 102
 Knapen J. H., James P. A., 2009, ApJ, 698, 1437
 Kravtsov A., Vikhlinin A., Meshcheryakov A., 2014, ArXiv: 1401.7329
 Labbé I., et al., 2010, ApJ, 716, L103
 Lilly S. J., Le Fevre O., Hammer F., Crampton D., 1996, ApJ, 460, L1
 Madau P., Pozzetti L., Dickinson M., 1998, ApJ, 498, 106
 Mannucci F., Cresci G., Maiolino R., Marconi A., Gnerucci A., 2010, MNRAS, 408, 2115
 Marinacci F., Pakmor R., Springel V., 2014, MNRAS, 437, 1750
 Michałowski M. J., Dunlop J. S., Cirasuolo M., Hjorth J., Hayward C. C., Watson D., 2012, A&A, 541, A85
 Michałowski M. J., Hayward C. C., Dunlop J. S., Bruce V. A., Cirasuolo M., Cullen F., Hernquist L., 2014, arXiv:1405.2335
 Mihos J. C., Hernquist L., 1996, ApJ, 464, 641
 Mitchell P. D., Lacey C. G., Cole S., Baugh C. M., 2014, arXiv:1403.1585
 Moster B. P., Naab T., White S. D. M., 2013, MNRAS, 428, 3121
 Nelson D., Vogelsberger M., Genel S., Sijacki D., Kereš D., Springel V., Hernquist L., 2013, MNRAS, 429, 3353
 Noeske K. G., Faber S. M., Weiner B. J., Koo D. C., Primack J. R., Dekel A., Papovich C., Conselice C. J., Floc'h E. L., Rieke G. H., Coil A. L., Lotz J. M., Somerville R. S., Bundy K., 2007, ApJ, 660, L47
 Patton D. R., Torrey P., Ellison S. L., Mendel J. T., Scudder J. M., 2013, MNRAS, 433, L59
 Pillepich A., et al., 2014, arXiv:1406.1174
 Porter L. A., Somerville R. S., Primack J. R., Johansson P. H., 2014, arXiv:1407.0594
 Rees M. J., Ostriker J. P., 1977, MNRAS, 179, 541
 Rodighiero G., et al., 2011, ApJ, 739, L40
 Sakamoto K., Wang J., Wiedner M. C., Wang Z., Peck A. B., Zhang Q., Petitpas G. R., Ho P. T. P., Wilner D. J., 2008, ApJ, 684, 957
 Salim S., et al., 2007, ApJS, 173, 267
 Sanders D. B., Soifer B. T., Elias J. H., Madore B. F., Matthews K., Neugebauer G., Scoville N. Z., 1988, ApJ, 325, 74
 Sargent M. T., Béthermin M., Daddi E., Elbaz D., 2012, ApJ, 747, L31
 Schawinski K., et al., 2014, MNRAS, 440, 889
 Schaye J., et al., 2010, MNRAS, 402, 1536
 Schaye J., et al., 2014, ArXiv:1407.7040
 Schmidt M., 1959, ApJ, 129, 243
 Scudder J. M., Ellison S. L., Torrey P., Patton D. R., Mendel J. T., 2012, MNRAS, 426, 549
 Sijacki D., Springel V., Di Matteo T., Hernquist L., 2007, MNRAS, 380, 877
 Sijacki D., Vogelsberger M., Kereš D., Springel V., Hernquist L., 2012, MNRAS, 424, 2999
 Silk J., 1977, ApJ, 211, 638
 Simha V., Weinberg D. H., Conroy C., Dave R., Fardal M., Katz N., Oppenheimer B. D., 2014, arXiv:1404.0402

- Speagle J. S., Steinhardt C. L., Capak P. L., Silverman J. D., 2014, arXiv:1405.2041, accepted to ApJS
- Springel V., 2010, MNRAS, 401, 791
- Springel V., Di Matteo T., Hernquist L., 2005, MNRAS, 361, 776
- Springel V., et al., 2005, Nature, 435, 629
- Springel V., Hernquist L., 2003, MNRAS, 339, 289
- Strateva I., et al., 2001, AJ, 122, 1861
- Toft S., et al., 2014, ApJ, 782, 68
- Torrey P., Cox T. J., Kewley L., Hernquist L., 2012, ApJ, 746, 108
- Torrey P., Vogelsberger M., Genel S., Sijacki D., Springel V., Hernquist L., 2014, MNRAS, 438, 1985
- Tremonti C. A., et al., 2004, ApJ, 613, 898
- Tully R. B., Fisher J. R., 1977, A&A, 54, 661
- Vogelsberger M., et al., 2014a, arXiv:1405.2921
- Vogelsberger M., et al., 2014b, Nature, 509, 177
- Vogelsberger M., Genel S., Sijacki D., Torrey P., Springel V., Hernquist L., 2013, MNRAS, 436, 3031
- Vogelsberger M., Sijacki D., Kereš D., Springel V., Hernquist L., 2012, MNRAS, 425, 3024
- Whitaker K. E., van Dokkum P. G., Brammer G., Franx M., 2012, ApJ, 754, L29
- White S. D. M., Rees M. J., 1978, MNRAS, 183, 341
- Wuyts S., et al., 2011, ApJ, 742, 96
- Zel'dovich Y. B., 1970, A&A, 5, 84